Single-frequency L5 attitude determination from IRNSS/NavIC and GPS a single- and dual-system analysis

Zaminpardaz, S; Teunissen, P. J.G.; Nadarajah, N

DOI
10.1007/s00190-017-1033-y

Publication date
2017

Document Version
Final published version

Published in
Journal of Geodesy

J Geod (2017) 91:1415–1433
DOI 10.1007/s00190-017-1033-y

ORIGINAL ARTICLE

Single-frequency L5 attitude determination from IRNSS/NavIC and GPS: a single- and dual-system analysis

S. Zaminpardaz[1] · **P. J. G. Teunissen**[1,2] · **N. Nadarajah**[1]

Received: 12 December 2016 / Accepted: 19 April 2017 / Published online: 3 May 2017

Abstract The Indian Regional Navigation Satellite System (IRNSS) has recently (May 2016) reached its full operational capability. In this contribution, we provide the very first L5 attitude determination analyses of the fully operational IRNSS as a standalone system and also in combination with the fully operational GPS Block IIF along with the corresponding ambiguity resolution results. Our analyses are carried out for both a linear array of two antennas and a planar array of three antennas at Curtin University, Perth, Australia. We study the noise characteristics (carrier-to-noise density, measurement precision, time correlation), the integer ambiguity resolution performance (LAMBDA, MC-LAMBDA) and the attitude determination performance (ambiguity float and ambiguity fixed). A prerequisite for precise and fast IRNSS attitude determination is the successful resolution of the double-differenced integer carrier-phase ambiguities. In this contribution, we will compare the performance of the unconstrained and the multivariate-constrained LAMBDA method. It is therefore also shown what improvements are achieved when the known body geometry of the antenna array is rigorously incorporated into the ambiguity objective function. As our ambiguity-fixed outcomes show consistency between empirical and formal results, we also formally assess the precise attitude determination performance for several locations within the IRNSS service area.

✉ S. Zaminpardaz
safoora.zaminpardaz@curtin.edu.au

[1] GNSS Research Centre, Department of Spatial Sciences, Curtin University, Perth, Australia

[2] Department of Geoscience and Remote Sensing, Delft University of Technology, Delft, The Netherlands

Keywords IRNSS · NavIC · GPS Block IIF · Integer carrier-phase ambiguity resolution · Attitude determination · Multivariate-constrained integer least squares · MC-LAMBDA

1 Introduction

Reaching the full operational capability recently (May 2016), the Indian Regional Navigation Satellite System (IRNSS) has been provided with the operational name of NavIC (Navigation with Indian Constellation). This new addition to GNSSs (Global Navigation Satellite Systems) has been developed by the Indian Space Research Organization (ISRO) with the objective of offering positioning, navigation and timing (PNT) to the users in its service area. Based on Code Division Multiple Access (CDMA), the IRNSS satellites transmit navigation signals on L5 (1176.45 MHz) with a binary phase shift key (BPSK (1)) modulation for standard positioning service (SPS) users, and with a binary offset carrier (BOC (5,2)) modulation for restricted service (RS) users (ISRO 2014). The fully operational IRNSS constellation consists of three geostationary orbit (GEO) satellites and four inclined geosynchronous orbit (IGSO) satellites (see Table 1), with the orbital period of one sidereal day (23 h and 56 min).

Transmission of L5 frequency by IRNSS makes it interoperable with three other GNSSs, i.e., GPS Block IIF, Galileo and QZSS, which share this frequency. At different stages of the IRNSS development, several studies have been published on the basis of IRNSS real data. Thoelert et al. (2014) assess the clock stability of satellite I1. Using the I1 and I2 observations, Kumari et al. (2015) test the accuracy of a precise model for solar radiation pressure, while Montenbruck and Steigenberger (2015) investigate the quality of the IRNSS navigation messages. The data of I1, I2 and I3 are used by

Table 1 Information on the IRNSS/NavIC satellites (ISRO 2016)

Satellite	Type	Longitude	Inclination	Launch date
IRNSS-1A (I1)	IGSO	55° E	29.0°	July 2013
IRNSS-1B (I2)	IGSO	55° E	31.0°	April 2014
IRNSS-1C (I3)	GEO	83° E	–	October 2014
IRNSS-1D (I4)	IGSO	111.75° E	30.5°	March 2015
IRNSS-1E (I5)	IGSO	111.75° E	28.1°	January 2016
IRNSS-1F (I6)	GEO	32.5° E	–	March 2016
IRNSS-1G (I7)	GEO	129.5° E	–	April 2016

Babu et al. (2015) for comparison of the orbit determination methods and by Chandrasekhar et al. (2015) to validate the orbit accuracy with modernized ephemeris parameters. The first positioning results based on the data of I1, I2, I3 and I4 over India are presented in Ganeshan et al. (2015) and over Australia in Zaminpardaz et al. (2016b). In 2010, following the launch of the first GPS Block IIF satellite, GPS started transmitting L5 signals as part of the GPS modernization (GPS Directorate 2011). With the launch of the last satellite of Block IIF on February 2016, it now has all its 12 satellites operational. There exist a few studies making use of the GPS L5 real data. An analysis of the GPS L5 stochastic properties through different GNSS observables combinations is provided by de Bakker et al. (2012), and the GPS L5-based precise point positioning (PPP) results are presented in Tegedor and Øvstedal (2014). The DISBs (differential inter-system biases) between GPS L5 and the same signal of the other systems including IRNSS are characterized in Odijk and Teunissen (2013) and Odijk et al. (2016).

In this contribution, we aim to investigate the L5-signal instantaneous attitude determination capability using the IRNSS as a standalone system and also in combination with the GPS Block IIF. Since L5 signal is a quite new addition to the GNSS signals, it is important to gain an understanding of its performance from the viewpoint of different applications like attitude determination. The attitude of a platform can be determined using multiple GNSS antennas which are rigidly mounted on it (Cohen 1992; Lu 1995; Madsen and Lightsey 2004; Psiaki 2006). Depending on the application at hand, this platform can be a vessel, a land vehicle, an aircraft or a space platform (Hodgart and Purivigraipong 2000; Li et al. 2004; Hide et al. 2007; Hauschild et al. 2008; Wang et al. 2009; Giorgi et al. 2010; Teunissen et al. 2011). Precise and fast GNSS-based attitude determination can be realized through incorporation of the very precise phase observations and hence requires the successful resolution of the double-differenced (DD) integer carrier-phase ambiguities. The Least-squares AMBiguity Decorrelation Adjustment (LAMBDA) method developed by Teunissen (1995, 1997, 1999) is the standard method used for solving the unconstrained mixed-integer GNSS models, which also results in the highest possible ambiguity resolution success rate (percentage of correctly fixed solutions).

However, if the local antenna geometry in the body frame is known, one can further improve the ambiguity resolution performance. To realize this, the multivariate-constrained (MC-)LAMBDA method has been developed (Park and Teunissen 2003, 2009; Teunissen 2006; Buist 2007; Giorgi et al. 2008; Giorgi and Buist 2008; Giorgi et al. 2010; Teunissen et al. 2011). This method incorporates the known local antenna geometry in a rigorous manner into the ambiguity objective function, leading to higher success rates as compared to the standard LAMBDA. The attitude determination performance of the L5 signal of IRNSS, GPS, Galileo and QZSS was assessed by Nadarajah et al. (2015). Their assessment was based on *two* IRNSS and *seven* GPS Block IIF satellites. Our attitude evaluations in the current study, however, employ, for the first time, the *fully operational* IRNSS and GPS Block IIF.

This contribution is organized as follows. In Sect. 2, the unconstrained and multivariate-constrained single-frequency GNSS model of observations is formulated. The measurement setup is explained in Sect. 3, while the noise characteristics of the IRNSS and GPS L5 signal are presented in Sect. 4 through the carrier-to-noise density, the estimated measurement precision and time correlation. Section 5 compares the ambiguity resolution performance on the basis of LAMBDA and MC-LAMBDA for both a linear and a planar array of GNSS antennas at Curtin University, Perth, Australia. In Sect. 6, an empirical and formal analysis of the instantaneous attitude determination performance at Perth is provided for the mentioned arrays. We then extend this study with formal analysis to the IRNSS service area. Finally, a summary and conclusions are given in Sect. 7.

2 GNSS model of observations

In this section, the dual-system (IRNSS + GPS) single-frequency GNSS model of observations for an array of antennas is formulated from which the single-system (IRNSS) model follows as a special case. We assume the array is

of small scale such that the differential atmospheric delays (troposphere and ionosphere) and orbital errors between the antennas can be neglected. Due to the close proximity of the antennas, the satellites elevations are considered to be the same for all the antennas. We further assume that all the receivers are of the same manufacturer (make, type and firmware), thus allowing us to assume that the IRNSS-GPS ISBs are zero (Odijk et al. 2012, 2016). Therefore, instead of classical double differencing per constellation, inter-system double differencing can be used, resulting in a higher level of redundancy. In the sequel, we refer to the IRNSS-specific parameters and the GPS-specific parameters using the subscripts $_I$ and $_G$, respectively.

2.1 Unconstrained model

Suppose that n antennas, firmly mounted on a platform, are simultaneously tracking m_I IRNSS plus m_G GPS satellites on L5 frequency with the wavelength of λ. With $m = m_I + m_G$, the multivariate linearized single-epoch DD GNSS array model of observations then reads

$$E\left[(D_m^T \otimes D_n^T)\begin{bmatrix}\phi\\ p\end{bmatrix}\right] = \begin{bmatrix} D_m^T G \otimes I_{n-1} & \lambda I_{m-1} \otimes I_{n-1} \\ D_m^T G \otimes I_{n-1} & 0 \end{bmatrix}\begin{bmatrix} vec(X^T) \\ a \end{bmatrix}$$
$$D\left[(D_m^T \otimes D_n^T)\begin{bmatrix}\phi\\ p\end{bmatrix}\right] = \begin{bmatrix} D_m^T Q_{\phi\phi} D_m \otimes D_n^T D_n & 0 \\ 0 & D_m^T Q_{pp} D_m \otimes D_n^T D_n \end{bmatrix} \quad (1)$$

where $E[.]$ and $D[.]$ denote the expectation and dispersion operator and $\otimes$ and $vec(.)$ denote Kronecker product and vec-operator (Harville 1997; Magnus and Neudecker 1995), respectively. The $(m-1)\times m$ matrix $D_m^T = [-e_{m-1},\ I_{m-1}]$ is the differencing matrix forming the between-satellite single differencing, while the $(n-1)\times n$ matrix $D_n^T = [-e_{n-1},\ I_{n-1}]$ forms the between-receiver single differencing. e and I are, respectively, the vector of ones and the identity matrix the dimension thereof is specified by their subscripts. The combined vectors and matrices can be split into system-specific parts as

$$\phi = \left[\phi_I^T, \phi_G^T\right]^T,\ p = \left[p_I^T, p_G^T\right]^T,\ G = \left[G_I^T, G_G^T\right]^T$$
$$Q_{\phi\phi} = \text{blkdiag}\left(\sigma_{\phi_I}^2 W_I^{-1},\ \sigma_{\phi_G}^2 W_G^{-1}\right)$$
$$Q_{pp} = \text{blkdiag}\left(\sigma_{p_I}^2 W_I^{-1},\ \sigma_{p_G}^2 W_G^{-1}\right)$$

With $* = \{I, G\}$, ϕ_* and p_* denote, respectively, the $m_* n$-vectors of the undifferenced "observed-minus-computed" phase and code observations of the following structure: $y_* = \{\phi_*, p_*\}$, $y_* = [y^{1_*^T},\ y^{2_*^T}, \ldots, y^{m_*^T}]^T$, with $y^{s_*} = [y_1^{s_*},\ y_2^{s_*}, \ldots, y_n^{s_*}]^T$ and with $y_r^{s_*}$ being the phase/code observation between antenna r and satellite s_*. The $m_* \times 3$ matrix $G_* = [-u^{1_*}, \ldots, -u^{m_*}]^T$ includes the undifferenced receiver-satellite unit direction vectors $u^{s_*^T}$ as its rows. The unknown baseline components in NED (North–East–Down) frame are included in the $3 \times (n-1)$ matrix X, and the unknown integer DD ambiguities, in cycle, in the $(m-1)(n-1)$-vector a. The zenith-referenced standard deviation of the undifferenced phase and code observables are denoted as σ_{ϕ_*} and σ_{p_*}, respectively. The $m_* \times m_*$ diagonal matrix $W_* = \text{diag}(w^{1_*}, \ldots, w^{m_*})$ captures the satellite elevation dependency of the GNSS observables. In this contribution, the satellite elevation-dependent weight w^{s_*} takes the form of the exponential weighting function as

$$w^{s_*} = \left[1 + 10\exp\left(-\frac{\theta^{s_*}}{10}\right)\right]^{-2} \quad (2)$$

where θ^{s_*} is the elevation of the satellite s_* in degrees (Euler and Goad 1991). To obtain the standalone IRNSS observational model from (1), it is enough to put $m_G = 0$. Since, in the case of a single epoch, the number of DD ambiguities equals that of the DD phase observables, uncorrelated with the DD code observables, the DD phase observables are fully reserved for the ambiguities estimation. Therefore, the single-epoch estimation of the baselines components does not benefit from the high precision phase observables unless the DD ambiguities are resolved to their integer values. Upon fixing the DD ambiguities, the phase observations act as the very precise code observations and improve the baseline estimation and precision. In the following, we use the system-specific indexes only when working with the dual-system model of observations.

2.2 Multivariate-constrained model

In the model of observations given by (1), the known antennas' geometry in the body frame is disregarded. Such information, if taken into account, can strengthen the GNSS observational model considerably. The baseline coordinates in the body frame B are linked to their counterparts in NED frame X through the following transformation (Teunissen 2007)

$$X = R\,B;\quad X,\ B \in \mathbb{R}^{3\times(n-1)},\ R \in \mathbb{O}^{3\times 3} \quad (3)$$

where $\mathbb{O}^{3\times 3}$ denotes the set of 3×3 matrices of which the column vectors form an orthonormal span. R is a rotation matrix satisfying $R^T R = I_3,\ \det(R) = +1$ (Kuipers 2002). Substituting (3) in (1), the unknown parameters and their corresponding design matrix change accordingly as

$$vec(X^T) \to vec(R^T);\quad D_m^T G \otimes I_{n-1} \to D_m^T G \otimes B^T \quad (4)$$

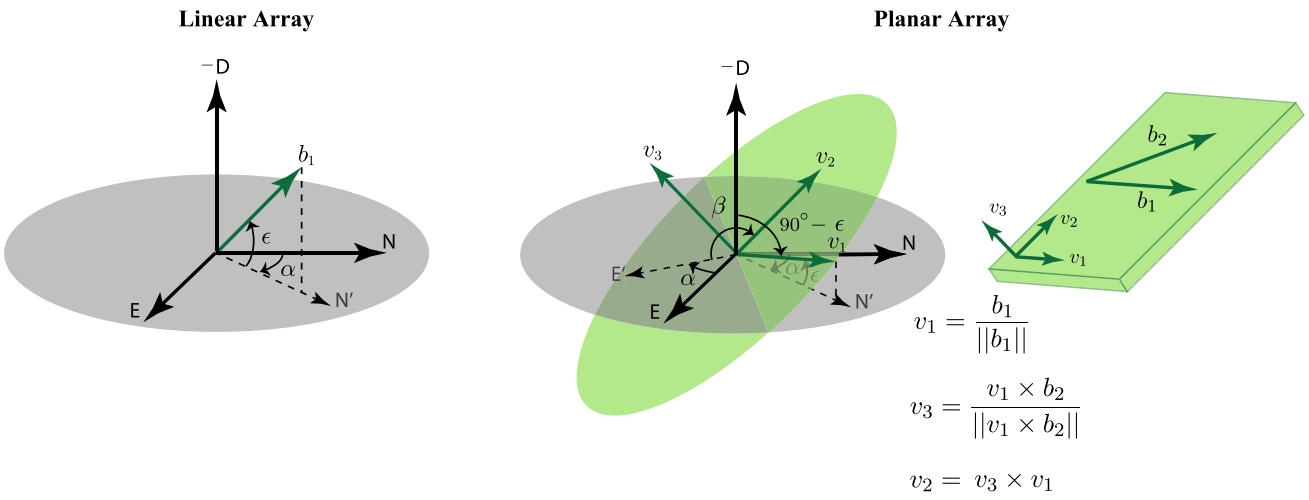

Fig. 1 Transformation between North–East–Down frame and the body frame of a linear array (b_1) and a planar array ($v_1,\ v_2,\ v_3$)

In (3), since the matrix R is of full rank, the matrices X and B are also of the same rank, namely $\text{rank}(X) = \text{rank}(B) = q$ which is the dimension of the space spanned by the baselines. The baselines achieve their full span if $q = \min(3, n-1)$ (Teunissen 2012). If $q < \min(3, n-1)$, the transpose of the baseline matrix B^T forming the design matrix $D_m^T G \otimes B^T$ would be rank deficient. In order to rule this case out, we assume that the body frame axes are formed by the first *three* baselines which are represented in the body frame as (Teunissen 2007, 2012)

$$[b_1,\ b_2,\ b_3] = \begin{bmatrix} b_{11} & b_{21} & b_{31} \\ 0 & b_{22} & b_{32} \\ 0 & 0 & b_{33} \end{bmatrix} \tag{5}$$

Therefore, (3) would be replaced by

$$X = R_q\, B; \quad X \in \mathbb{R}^{3\times(n-1)},\ B \in \mathbb{R}^{q\times(n-1)},\ R_q \in \mathbb{O}^{3\times q} \tag{6}$$

In which $R_q^T R_q = I_q$, and $\mathbb{O}^{3\times q}$ denotes the set of $3 \times q$ matrices of which the q column vectors form an orthonormal span. In the sequel, we will work with (6) instead of (3).

2.3 Ambiguity resolution and attitude determination

The aim of the attitude determination is to determine matrix R_q in (6) from which (some of) the attitude parameters, i.e., heading (α), elevation (ε) and bank (β), can be extracted. As an example, when $q = 3$, R_3 can be parametrized as

$$R_3 = \begin{bmatrix} c_\alpha c_\varepsilon & -s_\alpha c_\beta + c_\alpha s_\varepsilon s_\beta & s_\alpha s_\beta + c_\alpha s_\varepsilon c_\beta \\ s_\alpha c_\varepsilon & c_\alpha c_\beta + s_\alpha s_\varepsilon s_\beta & -c_\alpha s_\beta + s_\alpha s_\varepsilon c_\beta \\ -s_\varepsilon & c_\varepsilon s_\beta & c_\varepsilon c_\beta \end{bmatrix} \tag{7}$$

in which $c_{\{.\}} = \cos\{.\}$ and $s_{\{.\}} = \sin\{.\}$. For $q = 1,\ 2$, R_q is formed by the first column and the first two columns of R_3, respectively. Our analyses in this contribution are conducted for a linear array of one baseline and a planar array of two baselines. Figure 1 schematically shows how the body frame and therefore the attitude angles are defined for these two types of array. With the aid of this figure, (6) can be worked out for the *linear array* as

$$x_1 = ||b_1|| \begin{bmatrix} c_\alpha c_\varepsilon \\ s_\alpha c_\varepsilon \\ -s_\varepsilon \end{bmatrix} \tag{8}$$

and for the *planar array* as

$$[x_1\ \ x_2] = \begin{bmatrix} c_\alpha c_\varepsilon & -s_\alpha c_\beta + c_\alpha s_\varepsilon s_\beta \\ s_\alpha c_\varepsilon & c_\alpha c_\beta + s_\alpha s_\varepsilon s_\beta \\ -s_\varepsilon & c_\varepsilon s_\beta \end{bmatrix} \begin{bmatrix} ||b_1|| & \langle b_2, v_1\rangle \\ 0 & \langle b_2, v_2\rangle \end{bmatrix} \tag{9}$$

where $||.||$ and $\langle .,.\rangle$ denote the Euclidean norm and inner product, respectively.

Solving (1) in a least-squares sense considering the constraint in (6), the solutions for the integer ambiguity vector $\breve{a}$ and the orthonormal matrix $\breve{R}_q$ are given by Teunissen (2007)

$$\begin{aligned} \breve{R}_q(a) &= \underset{R_q\in\mathbb{O}^{3\times q}}{\text{argmin}} \left|\left|vec(\hat{R}_q(a) - R_q)\right|\right|^2_{Q_{vec(\hat{R}_q(a))}} \\ \breve{a} &= \underset{a\in\mathbb{Z}^{(m-1)\times(n-1)}}{\text{argmin}} \left(||\hat{a} - a||^2_{Q_{\hat{a}\hat{a}}} + \left|\left|vec(\hat{R}_q(a) - \breve{R}_q(a))\right|\right|^2_{Q_{vec(\hat{R}_q(a))}} \right) \\ \breve{R}_q &= \breve{R}_q(\breve{a}) \end{aligned} \tag{10}$$

where $vec(\hat{R}_q(a)) = vec(\hat{R}_q) - Q_{vec(\hat{R}_q)\hat{a}} Q^{-1}_{\hat{a}\hat{a}}(\hat{a} - a)$. $\hat{R}_q$ and $\hat{a}$ are the least-squares solutions disregarding the orthonormality of the rotation matrix and integerness of

the DD ambiguities, and $Q_{vec(\hat{R}_q)}$, $Q_{\hat{a}\hat{a}}$ and $Q_{vec(\hat{R}_q)\hat{a}}$ are their corresponding variance and covariance matrices. In the sequel, depending on which constraints are taken into account, we distinguish between the following scenarios

$R_q \in \mathbb{R}^{3\times q}$: unconstrained scenario;
$R_q \in \mathbb{O}^{3\times q}$: constrained scenario;
$a \in \mathbb{R}^{(m-1)\times(n-1)}$: ambiguity-float scenario;
$a \in \mathbb{Z}^{(m-1)\times(n-1)}$: ambiguity-fixed scenario.

The expression to be minimized in the second minimization problem of (10) is the ambiguity objective function which is nonstandard due to the presence of the second term. This term would disappear provided the orthonormality of the rotation matrix is disregarded. To solve the minimization problem in (10), the MC-LAMBDA method has been developed (Park and Teunissen 2003, 2009; Teunissen 2006, 2010; Buist 2007; Giorgi et al. 2008, 2010; Giorgi and Buist 2008; Teunissen et al. 2011), incorporating the orthonormality of the rotation matrix in a rigorous manner. This method therefore leads to higher success rates w.r.t. the standard LAMBDA which only takes into account the integerness of the DD ambiguities. The performance of both LAMBDA and MC-LAMBDA is investigated in Sect. 5.

As was mentioned, our evaluations in this study are conducted for a linear array of one baseline and a planar array of two baselines. For such a situation, matrix B would become invertible, and (10) can alternatively be written as (Teunissen 2012)

$$\begin{aligned}
\check{X}(a) &= \underset{\substack{X^TX = B^TB \\ X \in \mathbb{R}^{3\times(n-1)}}}{\operatorname{argmin}} \left|\left|vec\left(\hat{X}(a) - X\right)\right|\right|^2_{Q_{vec(\hat{X}(a))}} \\
\check{a} &= \underset{a\in\mathbb{Z}^{(m-1)\times(n-1)}}{\operatorname{argmin}} \left(||\hat{a} - a||^2_{Q_{\hat{a}\hat{a}}} + \left|\left|vec\left(\hat{X}(a) - \check{X}(a)\right)\right|\right|^2_{Q_{vec(\hat{X}(a))}}\right) \\
\check{X} &= \check{X}(\check{a})
\end{aligned} \tag{11}$$

For the single-baseline scenario, the constraint in the first expression of (11) is a constraint on the baseline length, i.e., $||x|| = l$. For such a situation, $\check{x}(a)$ is the vector on the sphere of radius l that has the smallest distance to $\hat{x}(a)$, where distance is measured with respect to the metric defined by the variance matrix $Q_{\hat{x}(a)\hat{x}(a)}$ (Teunissen 2010).

3 Measurement experiment

In this contribution, we investigate the L5-signal attitude determination performance based on standalone IRNSS and IRNSS + GPS Block IIF, for both the linear and planar arrays. The data are taken from three stations CUCC, CUBB and CUT3 of short baselines at Curtin University, Perth, Australia (Fig. 2a). Each station is equipped with a JAVAD TRE_G3TH_8 receiver and connected to a TRM59800.00 SCIS antenna. The dataset contains the 1-s (1Hz) IRNSS and GPS Block IIF L5 observations collected with a cutoff elevation angle of 10° on DOY (Day Of Year) 167 of 2016.

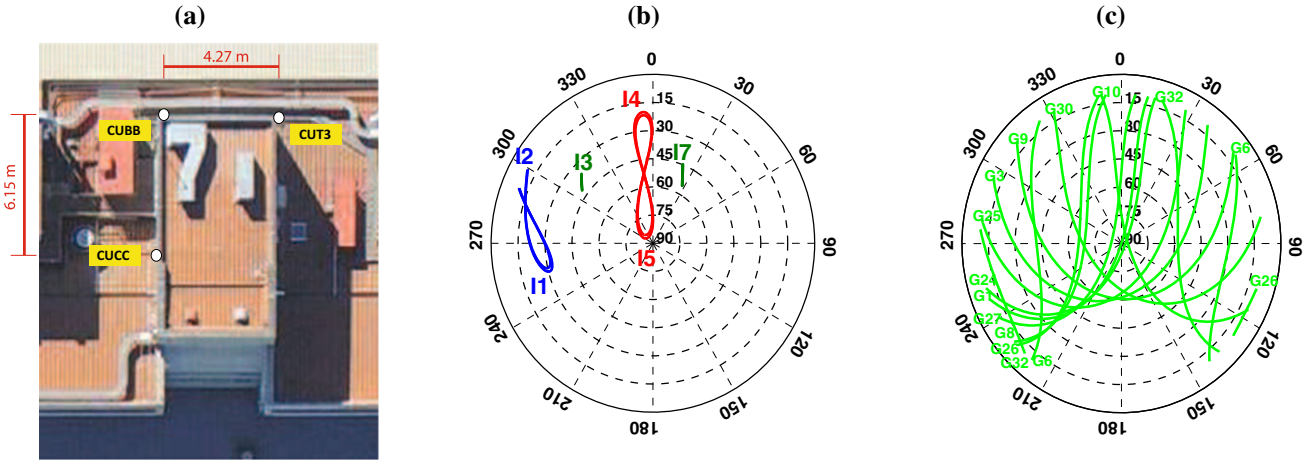

Fig. 2 Curtin University stations used with the corresponding skyplots. **a** CUCC, CUBB and CUT3 are equipped with JAVAD TRE_G3TH_8 receivers, connected to TRM59800.00 SCIS antennas. The 24-h skyplot of **b** IRNSS and **c** GPS Block IIF at Perth, Australia, on DOY 167 of 2016 with the cutoff elevation of 10°

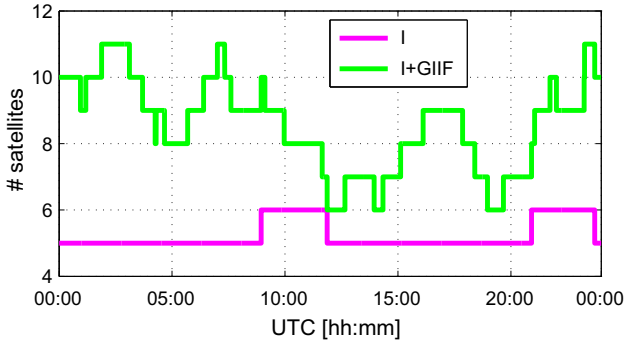

Fig. 3 Time series of the number of visible satellites of IRNSS (I) and IRNSS + GPS Block IIF (I + GIIF) at Perth, Australia, on DOY 167 of 2016 with the cutoff elevation of 10°

Figure 2b, c illustrates the 24-h skyplot of IRNSS and GPS Block IIF at Perth, respectively. Our analyses are conducted on an *epoch-by-epoch* basis, and since the satellites geometry has a low rate of change over time, our conclusions would be valid even for lower sampling rates, like 30 s. For both constellations, the broadcast ephemeris is used. Figure 3 shows the number of visible satellites for both the standalone IRNSS and IRNSS + GPS Block IIF. Combining IRNSS with GPS results in the number of visible satellites increasing from 5–6 to 6–11.

4 Noise characteristics

In this subsection, the noise characteristics of the L5 signal of IRNSS and GPS are assessed through the estimation of measurement precision, the carrier-to-noise density and time correlation. The zenith-referenced standard deviations in (1), i.e., $\{\sigma_{p_I}, \sigma_{\phi_I}, \sigma_{p_G}, \sigma_{\phi_G}\}$, capture the precision of the undifferenced phase and code observables and, if present, any remaining mis-modeled effects like multipath. Therefore upon eliminating the unwanted impact of multipath on the data, it is expected that these values experience improvement. In this study, the impact of multipath is eliminated through the method described in Zaminpardaz et al. (2016a). In order to see the impact of multipath, we apply the least-squares variance component estimation (LS-VCE) (Teunissen and Amiri-Simkooei 2008) to the 1-s L5 data of IRNSS and GPS collected on DOYs 175 and 176 of 2016 before and after applying multipath corrections. The mentioned standard deviations were estimated and the corresponding results are given in Table 2.

The code precision of the GPS L5 is significantly better than that of the IRNSS L5. This is also in agreement with the signature of the carrier-to-noise-density (C/N0) graphs of the two systems in Fig. 4. As it can be seen, the GPS L5 signal has larger values for C/N0 compared to the IRNSS L5. Upon multipath reduction, both IRNSS and GPS code standard deviations improve significantly. The phase observables of IRNSS L5 and GPS L5 are of comparable precisions and almost insensitive to the multipath correction. In the sequel, our analyses are based on both the original and the multipath-corrected data.

Table 2 LS-VCE estimation of the multipath-corrected and the original (within brackets) undifferenced phase σ_ϕ and code σ_p zenith-referenced standard deviations

Frequency	σ_p (cm)	σ_ϕ (mm)
IRNSS L5	19 (26)	1 (2)
GPS L5	7 (17)	1 (1)

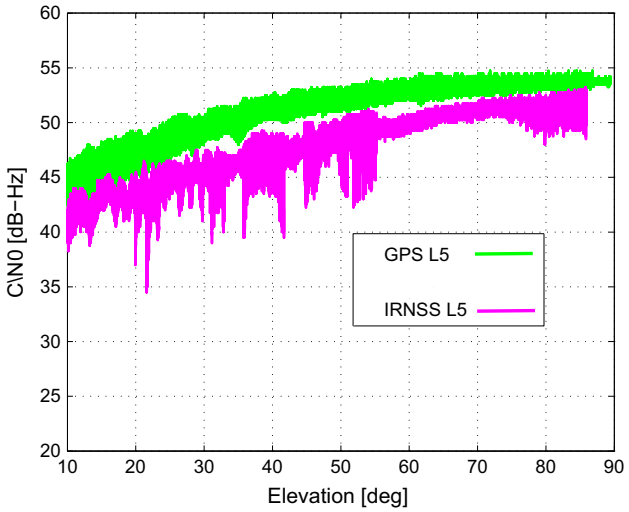

Fig. 4 Carrier-to-noise density (C/N0) for L5 signal of IRNSS and GPS Block IIF tracked by a JAVAD TRE_G3TH_8 receiver, connected to a TRM59800.00 SCIS antenna at Perth, Australia, on DOY 167 of 2016 with the cutoff elevation of 10°

Since 1-s data form the basis of our analyses, we assess the presence of time correlation in our data. Here we investigate the level of time correlation of the IRNSS and GPS L5 signals after and before applying multipath correction. Figure 5 (top) shows the graph of the time correlation among the original IRNSS L5 and GPS L5 observations as function of their time difference, while Fig. 5 (bottom) shows the same results for the multipath-corrected data. These graphs are based on applying the LS-VCE method (Amiri-Simkooei and Tiberius 2007) to 1 h of 1-s short-baseline data of CUCC–CUBB. A significant periodic time correlation among the original data is recognizable for both the IRNSS and GPS observations. Upon removing the multipath effect, however, the time correlation decreases dramatically and the periodic signature vanishes.

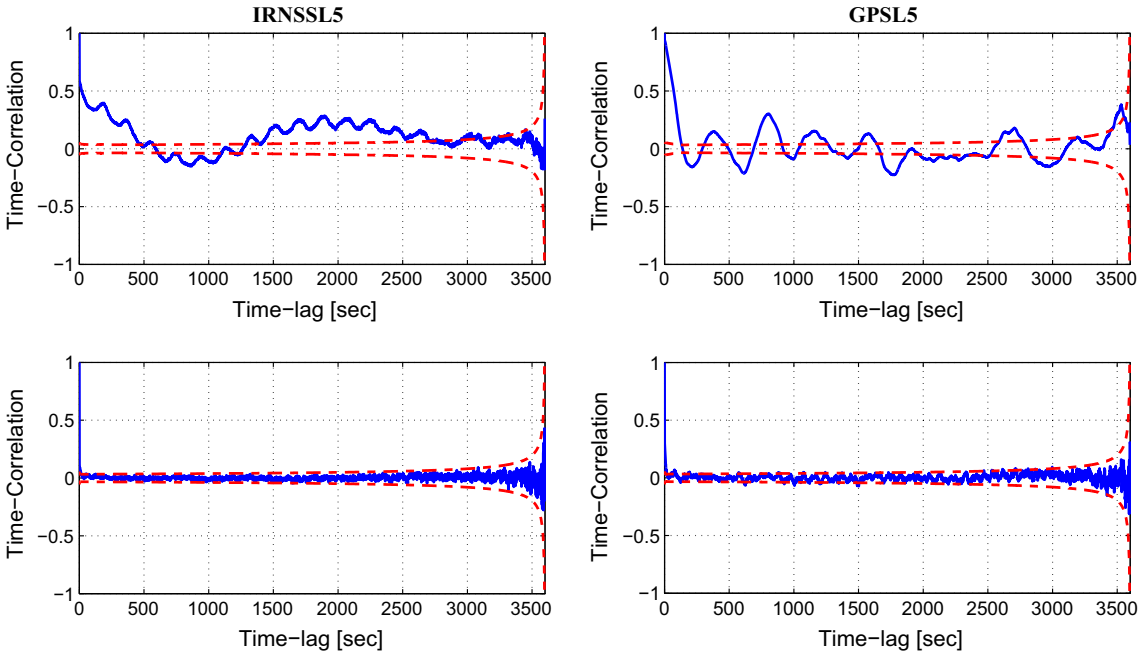

Fig. 5 Time correlation of the L5 signal of IRNSS and GPS Block IIF. Time series of the estimated time correlation among the 1-s short-baseline observations of the IRNSS L5 (*left*) and GPS Block IIF L5 (*right*). *Top* original data; *bottom* multipath-corrected data. The *red dashed lines* indicate the 95% formal confidence interval. The data were collected with the cutoff elevation of 10° by the stations CUCC and CUBB at Curtin University, Perth, Australia, on DOYs 175 and 176 of 2016

5 Ambiguity resolution performance

A prerequisite for precise and fast attitude determination is the successful resolution of the DD ambiguities. In this section, we will compare the performances of the standard LAMBDA and the MC-LAMBDA method, for both the standalone IRNSS L5 and IRNSS + GPS Block IIF L5. It is therefore also shown what improvements are achieved when the known body geometry of the antenna array is rigorously incorporated into the ambiguity objective function through MC-LAMBDA method. We consider two types of array: linear array formed by CUCC–CUBB and planar array formed by CUCC–CUBB–CUT3 (see Fig. 2). The body frame coordinate matrix B for the planar array is given by

$$B = \begin{bmatrix} 6.15 & 6.78 \\ 0 & 4.22 \end{bmatrix} \text{ m}$$

5.1 Standalone IRNSS

Figure 6 shows the 24-h time series of the IRNSS L5 single-epoch ambiguity-float and ambiguity-fixed solutions of the attitude angles corresponding to the linear array of CUCC–CUBB (a and b) and planar array of CUCC–CUBB–CUT3 (c and d). The fixed solutions on the left are estimated through LAMBDA, while those on the right are estimated through MC-LAMBDA. These results are computed based on the multipath-corrected GNSS data. In Table 3, however, we give the corresponding ambiguity resolution success rates on the basis of both the original and the multipath-corrected data. From this table, through either LAMBDA or MC-LAMBDA, multipath correction indeed improves the ambiguity resolution success rate for both the linear and planar array. This enhancement is, however, negligible (0.1%) in case of using the MC-LAMBDA method to resolve the planar array ambiguities. The advantage of MC-LAMBDA over LAMBDA is quite clear from the results in Table 3 and Fig. 6. Switching from LAMBDA to MC-LAMBDA, the success rate increases from 20.4 to 94.3% for the linear array and from 9.3 to 99.9% for the planar array. Higher MC-LAMBDA success rates would be achievable if we include the data of more than one epoch. Since the MC-LAMBDA success rate is already large, only a few number of epochs are needed to achieve higher success rates. This indicates that upon using MC-LAMBDA, standalone IRNSS can realize 24-h almost instantaneous precise attitude determination.

As the dimension of the array increases from one (linear) to two (planar), the LAMBDA success rate decreases while that of MC-LAMBDA increases. This is also shown in Fig. 6. The density of the red dots (wrongly fixed solutions) increases from panel (a) to (c), while it decreases from panel (b) to (d). In case of MC-LAMBDA which takes into account the constraint $X^T X = B^T B$, the model gets stronger from linear array to planar array due to the inclusion of larger

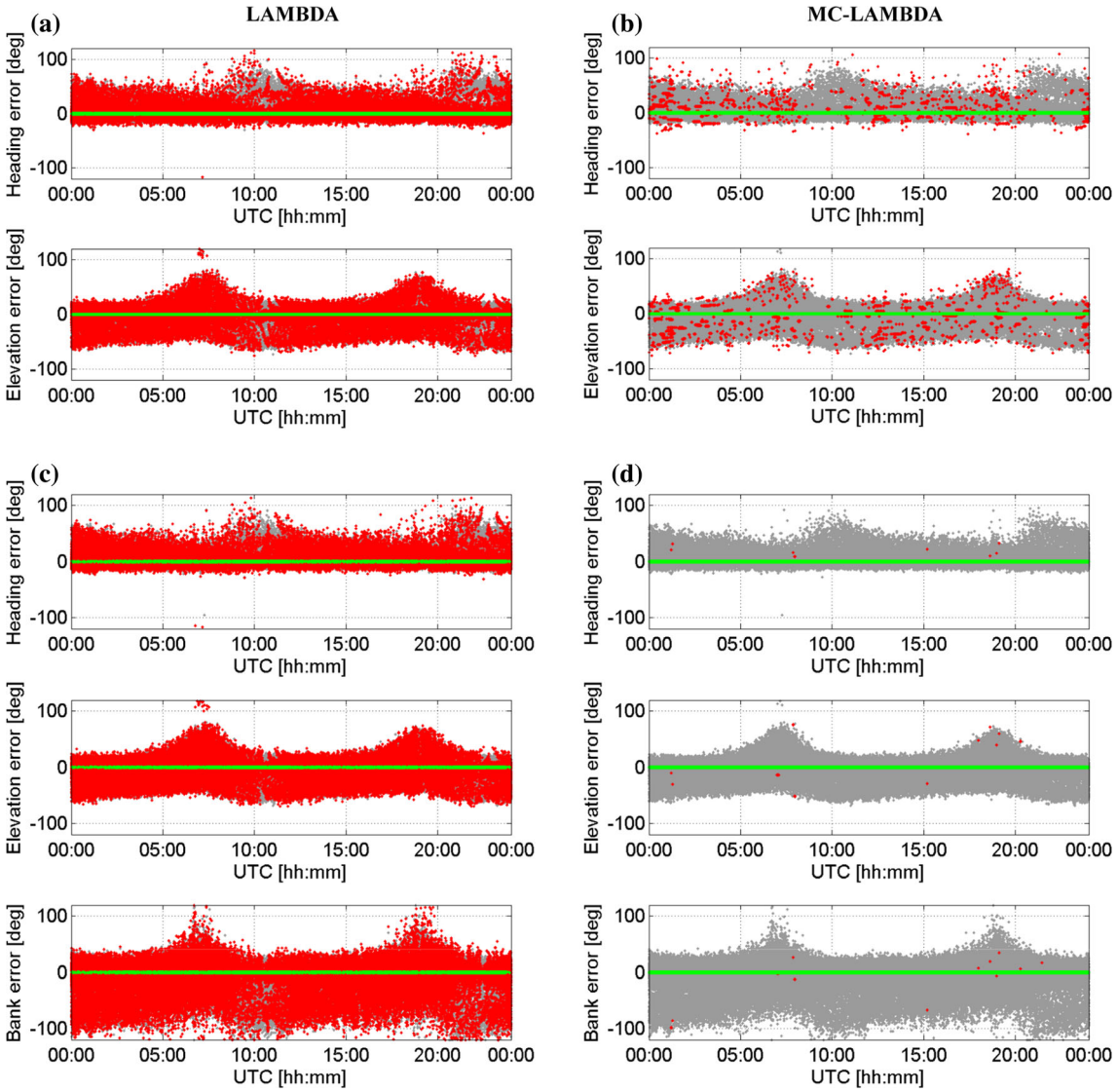

Fig. 6 Standalone IRNSS L5 instantaneous ambiguity resolution performance. Time series of the single-epoch solutions for the attitude angles based on the data collected on DOY 167 of 2016 at Perth with the cutoff elevation of 10°. *Each panel* shows three types of solution: *gray* ambiguity-float solutions; *red* wrongly fixed solutions; *green* correctly fixed solutions. The fixed solutions on the left are estimated through LAMBDA, while those on the right are estimated through MC-LAMBDA. **a**, **b** Correspond to the linear array formed by CUCC–CUBB. **c**, **d** Correspond to the planar array formed by CUCC–CUBB–CUT3

number of constraints which in turn leads to the ambiguity resolution improvements. The LAMBDA success rate for the single-frequency DD ambiguities corresponding to n antennas and m satellites can be well approximated by Teunissen (1998)

$$Ps \approx \left[2\Phi\left(\frac{1}{\mathrm{ADOP}}\right) - 1\right]^{(m-1)(n-1)} \tag{12}$$

where $\Phi(x) = \int_{-\infty}^{x} \frac{1}{\sqrt{2\pi}} \exp\{-\frac{1}{2}v^2\}\mathrm{d}v$. ADOP (ambiguity dilution of precision) is defined as the square root of the determinant of the ambiguity variance matrix raised to the power of one over the ambiguity dimension, and is the geometric average of the conditional ambiguities standard deviations (Teunissen 1997). For the observational model in (1), it can be shown that the ADOP corresponding to $n = 2$ is only 1.07 times larger than the ADOP corresponding to $n = 3$, which can be considered almost the same. Moreover, for a given value of ADOP, the success rate in (12) decreases as n increases. Therefore, from the linear array of two antennas to the planar array of three antennas, where ADOP remains almost unchanged but n increases from 2 to 3, the LAMBDA success rate is indeed expected to experience a reduction.

Table 3 Instantaneous L5 ambiguity resolution empirical success rate (%) for attitude observational model using the multipath-corrected data and the original data (within brackets)

Scenario	IRNSS L5		IRNSS + GPS Block IIF L5	
	LAMBDA	MC-LAMBDA	LAMBDA	MC-LAMBDA
Linear array	20.4 (15.2)	94.3 (89.8)	97.4 (95.1)	99.8 (99.8)
Planar array	9.3 (5.8)	99.9 (99.8)	97.1 (93.7)	>99.9 (>99.9)

The results are given for the linear array of CUBB–CUCC and the planar array of CUBB–CUCC–CUT3 (see Fig. 2)

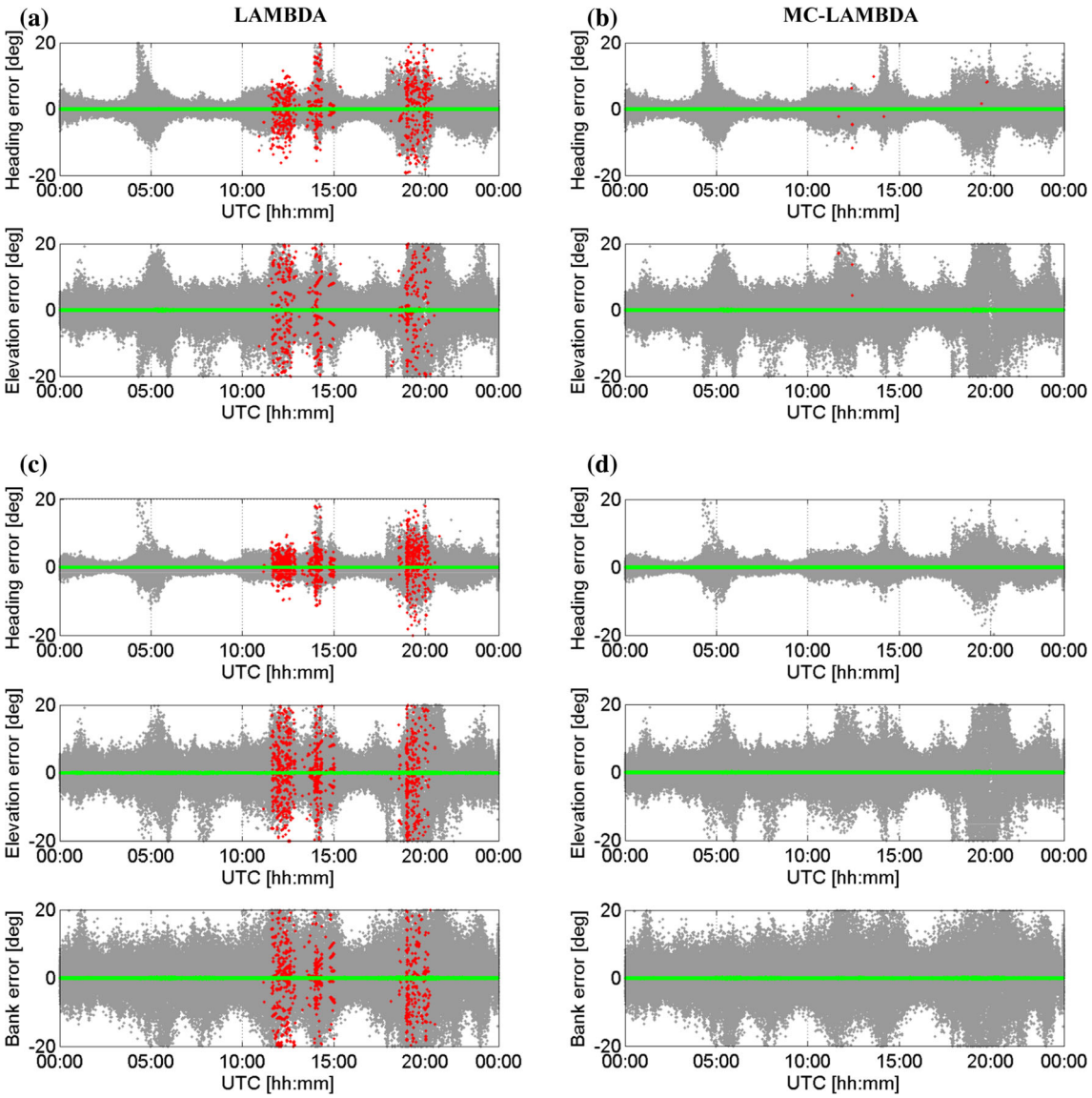

Fig. 7 IRNSS + GPS Block IIF L5 instantaneous ambiguity resolution performance. Time series of the single-epoch solutions for the attitude angles based on the data collected on DOY 167 of 2016 at Perth with the cutoff elevation of 10°. *Each panel* shows three types of solution: *gray* ambiguity-float solutions; *red* wrongly fixed solutions; *green* correctly fixed solutions. The fixed solutions on the left are estimated through LAMBDA, while those on the right are estimated through MC-LAMBDA. **a**, **b** Correspond to the linear array formed by CUCC–CUBB. **c**, **d** Correspond to the planar array formed by CUCC–CUBB–CUT3

5.2 IRNSS combined with GPS

Now we consider the dual-system scenario, i.e., IRNSS + GPS Block IIF. Figure 7 shows the corresponding dual-system counterparts of Fig. 6, for which the empirical ambiguity resolution success rates are also given in Table 3. According to this table, the impact of multipath correction on the ambiguity resolution performance is not very consider-

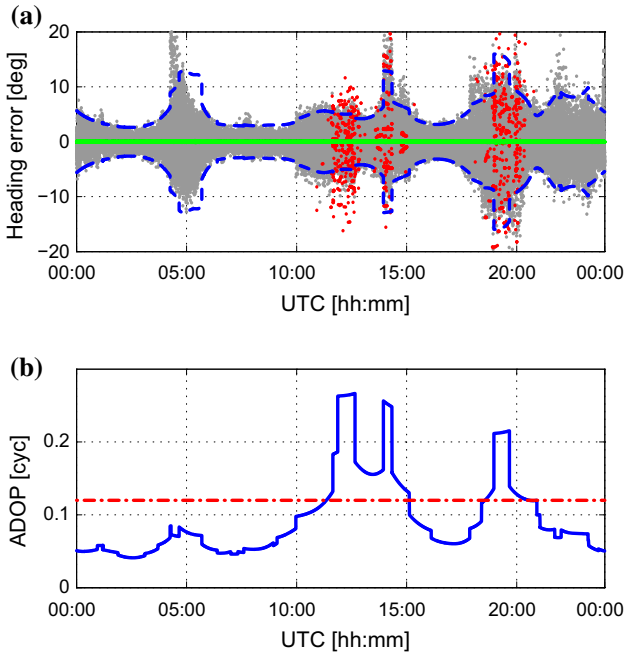

Fig. 8 **a** Time series of IRNSS + GPS Block IIF L5 instantaneous heading solutions based on the data of CUCC–CUBB collected on DOY 167 of 2016 at Perth with the cutoff elevation of 10°. *gray* ambiguity-float solution; *green* LAMBDA-based correctly fixed solution; *red* LAMBDA-based wrongly fixed solution. The *blue dashed lines* indicate the 95% formal confidence interval. **b** The corresponding time series of the single-epoch unconstrained ADOP (*blue*) and the value of 0.12 cycle (*red dashed line*)

able, particularly in case of MC-LAMBDA. As a result of the integration of the IRNSS with GPS Block IIF, the number of wrongly fixed solutions decreases dramatically particularly using the standard LAMBDA method. It can be seen that using MC-LAMBDA method, a success rate of 99.8% for the linear array and higher than 99.9% for the planar array can be attained.

In Figs. 6 and 7, the fluctuations in the ambiguity-float solutions (gray dots) and the variability of the wrongly fixed solutions (red dots) density can be explained through, respectively, the (linearized) formal standard deviations and the ADOP. Here, as an example, we explain the behavior of the heading dual-system estimations based on the linear array. The information depicted in Fig. 8a are those in the top panel of Fig. 7a plus the 95% formal confidence interval based on the linearized formal ambiguity-float heading standard deviation (blue dashed lines). The signature of the blue lines is in agreement with that of the ambiguity-float heading error time series. Comparing the time series of the ambiguity-fixed heading solutions with that of the ADOP (blue graph) shown in Fig. 8b, the wrong ambiguity fixing occurs during the periods of large ADOPs. The red dashed line in this figure indicates the ADOP value of 0.12 cycle. As a rule of thumb, an ADOP smaller than about 0.12 cycle corresponds to a LAMBDA success rate of larger than 99.9% (Odijk and Teunissen 2008).

6 Attitude determination performance

Having investigated the ambiguity resolution performance, we now turn our focus onto the attitude determination performance. In this section, we present our numerical evaluations of the L5-signal attitude determination performance for standalone IRNSS and IRNSS integrated with GPS Block IIF, for the aforementioned linear and planar array.

6.1 Standalone IRNSS

We start our attitude determination analysis with the linear array of CUCC–CUBB. Figure 9 illustrates for this array in a stepwise manner how the baseline solutions are built up from unconstrained ambiguity-float scenario to the constrained ambiguity-fixed scenario. The gray vector and sphere shown in all the panels of this figure are the baseline ground truth and the sphere with the radius of the baseline (CUCC–CUBB) length l, respectively. Figure 9a shows the single-epoch IRNSS L5 baseline solutions as blue dots for the unconstrained ambiguity-float scenario. The dispersion in the baseline solutions is governed by the code precision and satellites geometry. The excursions in this three-dimensional scatter plot are due to the significant change that the receiver-satellite geometry undergoes during a 24-h period.

Shown in Fig. 9b are the single-epoch IRNSS L5 baseline solutions for the constrained ambiguity-float scenario (gray dots). As is shown, upon constraining the baseline length $||x|| = l$, the corresponding solutions can only vary on a sphere with the radius of l. Incorporating the integerness of the DD ambiguities, Fig. 9c illustrates the single-epoch IRNSS L5 solutions for the constrained ambiguity-fixed scenario (green dots: correctly fixed; red dots: wrongly fixed). For this scenario, there are different clusters of the baseline solutions which correspond to different estimated integer values for the DD ambiguities. The green cluster associates with the correct integer value comprising 94.3% of the fixed solutions, while the red clusters correspond to the wrong integer values. To judge whether a DD ambiguity is correctly fixed, its corresponding integer solution is compared with the reference integer DD ambiguity computed based on the multi-epoch solution of the baseline-known model.

Figure 10a shows the horizontal scatter plot of the single-epoch IRNSS L5 baseline solutions, corrected for the baseline ground truth, for all the scenarios depicted in Fig. 9. Looking at the blue scatter plot, a Northwest elongation can be recognized which is due to a specific receiver-satellite geometry. In order to explain this, we make use of the confidence ellipse concept as it is the formal representative

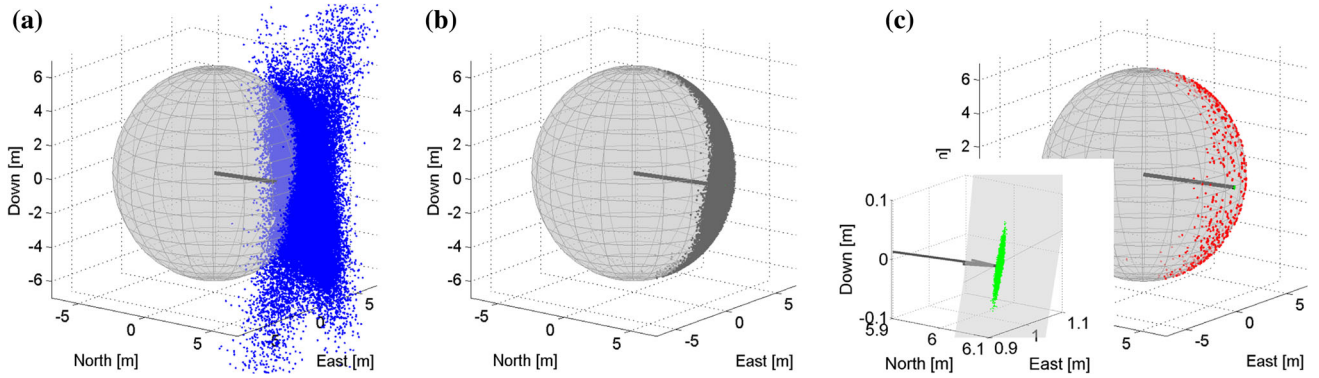

Fig. 9 Single-epoch IRNSS L5 solutions of the CUCC–CUBB baseline at Curtin University on DOY 167 of 2016 with the cutoff elevation of 10°. **a** Unconstrained ambiguity-float scenario; **b** Constrained ($||x|| = l$) ambiguity-float scenario; **c** Constrained ($||x|| = l$) ambiguity-fixed scenario (with a zoom-in in the lower left). *The gray vector* and the sphere shown in all the three panels denote, respectively, the baseline ground truth and the sphere with the radius of the CUCC–CUBB baseline length l. In panel **c**, *green and red dots* show the correctly fixed and wrongly fixed solutions, respectively

of the empirical scatter plot. Denoting the unconstrained ambiguity-float baseline solution as $\hat{x}$ with mean and covariance matrix of, respectively, x and $Q_{\hat{x}\hat{x}}$, its confidence ellipse reads

$$(\hat{x} - x)^T Q_{\hat{x}\hat{x}}^{-1} (\hat{x} - x) = k^2 \tag{13}$$

in which the constant k^2 is chosen such that a certain confidence level, e.g., 95%, is reached. As the direction of elongation is given by the direction of the eigenvector of $Q_{\hat{x}\hat{x}}^{-1}$ corresponding to its smallest eigenvalue, it follows with the aid of (1) that this direction is given by

$$\begin{aligned} f &= \underset{\tilde{f}}{\text{argmin}}\ \tilde{f}^T Q_{\hat{x}\hat{x}}^{-1} \tilde{f} \\ &= \underset{\tilde{f}}{\text{argmin}} \sum_{s=1}^{m} w^s \left[\tilde{f}^T \left(u^s - \bar{u} \right) \right]^2 \end{aligned} \tag{14}$$

with u^s being the unit direction vector from receiver to satellite s and $\bar{u}$ being the weighted average of the vectors u^s $(s = 1, \ldots, m)$. Note that here for simplicity, we drop the index $_I$ from those IRNSS-specific parameters. Figure 10b depicts the day-averaged skyplot position of the IRNSS satellites as well as that of the weighted average at Perth on DOY 167 of 2016 with the cutoff elevation of 10°. The differences $(u^s - \bar{u})$ are mainly oriented along the West–East direction. However, they have a non-negligible projection onto the North–South direction for satellites I1 and I2 such that the direction f that minimizes the contribution of all $(u^s - \bar{u})$ to (14) will mainly lie in an almost Northwesterly direction. This explains the Northwesterly elongation of the blue horizontal scatter plot in Fig. 10a.

The gray dots in Fig. 10a show the horizontal scatter plot of the constrained ambiguity-float baseline solutions, while the green and red dots show that of the constrained correctly and wrongly fixed baseline solutions, respectively. A zoom-in is also provided on the lower left of the figure to show the correctly fixed results more clearly. As it can be seen, the gray dots mainly take negative values along the North direction revealing that the constrained ambiguity-float baseline solutions are biased. This bias is due to the nonlinearity involved in the model of observations, called *nonlinearity bias* (Teunissen 1989). The nonlinearity of our model of observations stems from the orthonormality constraint of the rotation matrix R_q in (6). In "Appendix", we have elaborated more on this type of bias. The level of nonlinearity of the observational model depends on the baseline length and the GNSS data precision. The more precise the GNSS data and/or the longer the baseline, the less the impact of the constraint nonlinearity. Consider, as an example, the ambiguity-fixed scenario where the DD ambiguities are successfully fixed to their integer values. Then it is the very precise phase observations which take the leading role in baseline estimation. Therefore, the nonlinearity bias in the constrained correctly fixed solutions is expected to be negligible. This is indeed confirmed by the correctly fixed solutions scatter plot (green dots) in Fig. 10a.

Table 4, for the linear and planar array, lists the IRNSS L5 single-epoch empirical and formal standard deviations of the attitude angles based on the multipath-corrected data. In Sect. 5, it was shown that the instantaneous MC-LAMBDA ambiguity resolution using the standalone IRNSS is feasible with a notably high success rate. Therefore, Table 4 shows, in addition to the ambiguity-float results, the corresponding MC-LAMBDA ambiguity-fixed results as well. The empirical values are obtained from the single-epoch least-squares estimations of the attitude angles, whereas the formal values are obtained from taking the average of all the single-epoch

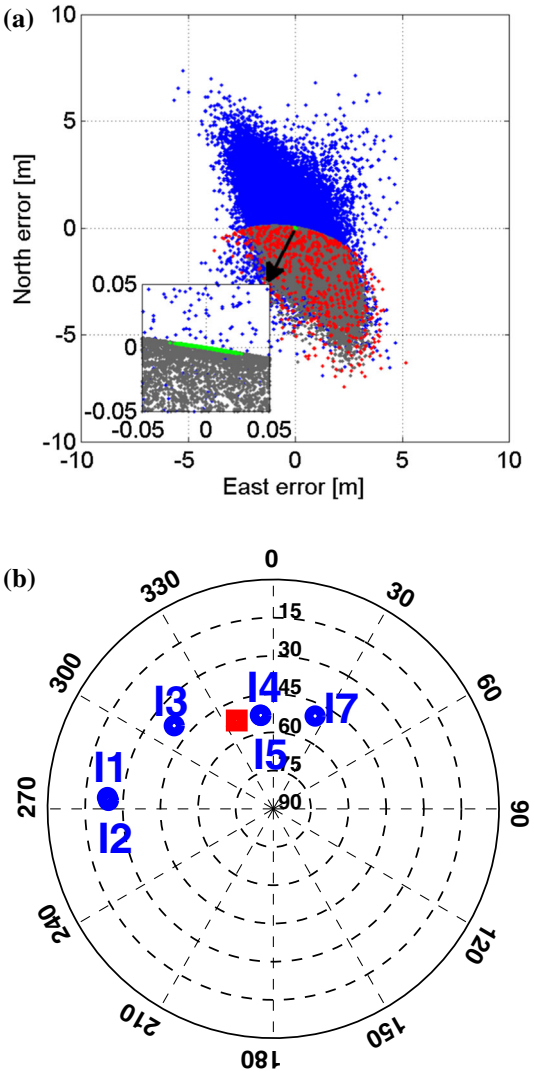

Fig. 10 **a** Single-epoch IRNSS L5 horizontal scatter plot of the CUCC–CUBB baseline at Curtin University corrected for the corresponding ground truth, on DOY 167 of 2016 with the cutoff elevation of 10°. *Blue* unconstrained ambiguity-float solutions; *gray* constrained ambiguity-float solutions; *red* constrained wrongly fixed solutions; *green* constrained correctly fixed solutions. A zoom-in is also depicted in the lower left of the figure. **b** Day-averaged IRNSS skyplot at Perth for DOY 167 of 2016 with the cutoff elevation of 10°. The *red square* indicates the skyplot position of vector $\bar{u}$ (cf. 14)

formal least-squares standard deviations based on the *linearized* observational model (w.r.t. the attitude angles). In case of the planar array, in addition to heading and elevation, bank is also estimable.

Comparing the empirical and the linearized formal results of the ambiguity-float scenario, an inconsistency is recognizable between them which can be attributed to the nonlinearity of the observational model. More explanation is provided in "Appendix". Upon fixing the DD ambiguities, however, the discrepancy between the empirical and the linearized formal outcomes disappears. The attitude angles standard deviations increase from heading to elevation to bank. This can be explained through the baselines orientation along with the IRNSS satellites geometry. Here, as an example, we consider the linear array of CUCC–CUBB with the baseline length of l. Through the linear approximation of (1) w.r.t. the attitude angles $\gamma = [\alpha \quad \varepsilon]^T$, the heading–elevation covariance matrix is given by

$$Q_{\hat{\gamma}\hat{\gamma}} = \frac{\sigma_p^2}{l^2}\left(\sum_{s=1}^{m} w^s \left[J^T\left(u^s - \bar{u}\right)\right]\left[J^T\left(u^s - \bar{u}\right)\right]^T\right)^{-1} \tag{15}$$

with J being the Jacobian matrix of the following form

$$J = [J_\alpha \quad J_\varepsilon] = \begin{bmatrix} -s_\alpha c_\varepsilon & -c_\alpha s_\varepsilon \\ c_\alpha c_\varepsilon & -s_\alpha s_\varepsilon \\ 0 & -c_\varepsilon \end{bmatrix} \tag{16}$$

From (15) and (16), if $J_\alpha^T(u^s - \bar{u})$ is larger than $J_\varepsilon^T(u^s - \bar{u})$, then the heading estimation would be more precise than the elevation and vice versa. For the CUCC–CUBB baseline with almost the South–North orientation, we have $J_\alpha \approx [0,\ 1,\ 0]^T$ (East direction) and $J_\varepsilon \approx [0,\ 0,\ -1]^T$ (Up direction). Since the GNSS satellites have a larger extension along the horizontal plane than the vertical, heading is expected to have better precision than elevation. Equation (15) in addition reveals that the longer the baseline, the more precise the attitude angles estimation.

Note, in case of working with the original data (without multipath correction), the ambiguity-fixed attitude angles standard deviations in Table 4 change as follows. The value of σ_{ϕ_l} for the original phase data is larger than that of the multipath-corrected phase data by a factor of 2 (see Table 2).

Table 4 Instantaneous IRNSS L5 attitude precision

Scenario	Ambiguity float (°)			Ambiguity fixed (°)		
	$\sigma_{\hat{\alpha}}$	$\sigma_{\hat{\varepsilon}}$	$\sigma_{\hat{\beta}}$	$\sigma_{\check{\alpha}}$	$\sigma_{\check{\varepsilon}}$	$\sigma_{\check{\beta}}$
Linear array						
emp	12.06	18.55	–	0.04	0.08	–
form	7.51	18.52	–	0.04	0.09	–
Planar array						
emp	11.77	18.97	27.64	0.03	0.07	0.10
form	6.54	17.01	21.92	0.03	0.08	0.10

Empirical and linearized formal standard deviations of the attitude angles in degrees for the linear array of CUBB–CUCC and the planar array of CUBB–CUCC–CUT3 (see Fig. 2), based on the multipath-corrected data collected on DOY 167 of 2016 with the cutoff elevation of 10°. The ambiguity-fixed solutions are obtained through applying MC-LAMBDA. emp, empirical; form, formal. $\sigma_{\hat{\alpha}}/\sigma_{\check{\alpha}}$, $\sigma_{\hat{\varepsilon}}/\sigma_{\check{\varepsilon}}$, $\sigma_{\hat{\beta}}/\sigma_{\check{\beta}}$, ambiguity-float/ambiguity-fixed standard deviation of heading, elevation and bank, respectively

Table 5 Instantaneous IRNSS + GPS Block IIF L5 attitude precision

Scenario	Ambiguity-float (°)			Ambiguity-fixed (°)		
	$\sigma_{\hat{\alpha}}$	$\sigma_{\hat{\varepsilon}}$	$\sigma_{\hat{\beta}}$	$\sigma_{\check{\alpha}}$	$\sigma_{\check{\varepsilon}}$	$\sigma_{\check{\beta}}$
Linear array						
emp	2.78	6.06	–	0.02	0.05	–
form	3.36	7.46	–	0.02	0.05	–
Planar array						
emp	1.93	5.69	8.76	0.01	0.04	0.06
form	2.07	6.28	9.15	0.01	0.04	0.06

Empirical and linearized formal standard deviations of the attitude angles in degrees for the linear array of CUBB–CUCC and the planar array of CUBB–CUCC–CUT3 (see Fig. 2), based on the multipath-corrected data collected on DOY 167 of 2016 with the cutoff elevation of 10°. The ambiguity-fixed solutions are obtained through applying MC-LAMBDA. emp, empirical; form, formal. $\sigma_{\check{\alpha}}/\sigma_{\hat{\alpha}}$, $\sigma_{\check{\varepsilon}}/\sigma_{\hat{\varepsilon}}$, $\sigma_{\check{\beta}}/\sigma_{\hat{\beta}}$, ambiguity-float/ambiguity-fixed standard deviation of heading, elevation and bank, respectively

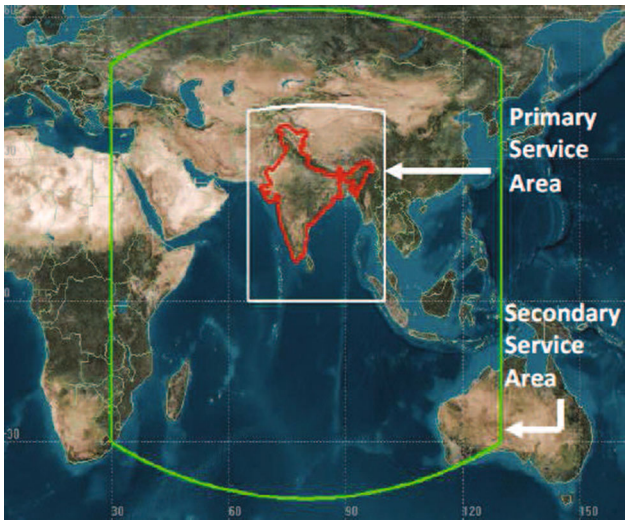

Fig. 11 IRNSS primary and secondary service area (image credit: ISRO)

However, the weight matrix corresponding to the multipath-corrected data is 2 times larger than that of the original data due to the adding multipath corrections based on the previous day data. Therefore, multiplying the ambiguity-fixed entries of Table 4 by $\sqrt{2}$ gives their counterparts on the basis of the original data.

6.2 IRNSS combined with GPS

Now we analyze the IRNSS L5 attitude determination capability when combined with GPS L5. Table 5 displays the dual-system counterparts of the entries in Table 4. Upon integrating IRNSS with GPS Block IIF, the attitude angles precisions improve by 3–4 times in case of ambiguity-float scenario and 1.5–2 times in case of ambiguity-fixed scenario. This improvement is due to the increase in number of visible satellites and, in case of ambiguity-float scenario, to the higher precision of the GPS L5 code observations w.r.t the IRNSS. As was explained for the standalone IRNSS scenario, following successful fixing of the ambiguities, the empirical and the linearized formal results become consistent with each other.

6.3 Attitude determination over the IRNSS service area

So far, we have presented the single-epoch formal and empirical analyses on the basis of the data collected at Perth. For the ambiguity-fixed scenario, a good consistency was shown between our empirical outcomes and their linearized formal counterparts (see Tables 4, 5). This agreement implies that the easy-to-compute (linearized) formal values can indeed be used to predict the expected attitude determination performance. Therefore, in this subsection, we perform a formal analysis of the ambiguity-fixed attitude angles standard deviations for a linear array of two antennas over the IRNSS primary and secondary service area, i.e., locations within $(-30° < \phi < 50°, 30° < \lambda < 130°)$. The extent of these two service areas is depicted in Fig. 11.

Prior to our ambiguity-fixed analyses, it is important to first investigate whether high instantaneous MC-LAMBDA success rates are achievable for the locations inside the IRNSS service area. To do so, we first compare the instantaneous LAMBDA formal success rate at these locations with that at Perth. If for a location, instantaneous LAMBDA success rate not lower than that at Perth can be achieved, then it can be concluded that the instantaneous MC-LAMBDA success rate at this location would also not be lower than its counterpart at Perth, which is as high as 90% for a linear array of two antennas (see Table 3). With this in mind, the standalone IRNSS ambiguity-fixed results are then given only for the locations with the larger instantaneous LAMBDA success rate than that at Perth.

Integration of the IRNSS with the GPS Block IIF results in the instantaneous LAMBDA success rate becoming higher than 70% for all the locations within $(-30° < \phi < 50°, 30° < \lambda < 130°)$. This means that these locations are expected to have the instantaneous MC-LAMBDA success rate higher than *at least* 70%. Therefore, the IRNSS + GPS Block IIF ambiguity-fixed results are given for all these locations.

Our ambiguity-fixed evaluations in this section are based on the variance matrix given in (15), albeit with σ_p being replaced by σ_ϕ. The precision with which the attitude angles can be estimated depends on the phase data precision [σ_ϕ], satellites geometry [u^s (receiver-satellite unit direction vector), w^s (satellite elevation-dependent weight)], baseline length [l] and orientation [α (heading), ε (elevation)]. For our analyses, we consider the following setup:

$\sigma_{\phi_I} = \sigma_{\phi_G} = 2$mm, baseline length $l = 1$m, baseline orientations ($\alpha = 0°,\ \varepsilon = 0°$), ($\alpha = 90°,\ \varepsilon = 0°$) and ($\alpha = 0°,\ \varepsilon = 45°$). For such a setup, Figs. 12 and 13 provide the color map of the day-averaged single-epoch ambiguity-resolved L5-based heading and elevation standard deviations on the basis of standalone IRNSS and IRNSS + GPS Block IIF, respectively. For other values of phase data precision and baseline length, the results of these figures will change according to (15). The white areas in Fig. 12 denote those locations excluded from our computations, due to having the poorer instantaneous MC-LAMBDA success rate than that of Perth. In order for the color maps to be readable, we use the same color to show all the elevation standard deviations not lower than 1.3°, and also the same color to illustrate all the heading standard deviations not lower than 0.9°.

The results in Figs. 12 and 13 show that the heading and elevation precision at a given location varies with changing baseline orientation. As was explained earlier, what drives the heading and elevation precision is the satellites extension along the vectors J_α and J_ε in (16), respectively. For the baseline orientations of ($\alpha = 0°,\ \varepsilon = 0°$) and ($\alpha = 90°,\ \varepsilon = 0°$), vector J_ε will always points toward Up direction, while vector J_α points toward East and South direction, respectively. Therefore, if the satellites have a larger extension along West–East compared to South–North, the heading corresponding to the baseline ($\alpha = 0°,\ \varepsilon = 0°$) will be more precise than that of ($\alpha = 90°,\ \varepsilon = 0°$). For example, for the location ($\phi = -30°, \lambda = 115.5°$) which is close to Perth, the standalone IRNSS heading associated with the baseline orientation ($\alpha = 0°,\ \varepsilon = 0°$) is about 1.4 times more precise than that of the baseline orientation ($\alpha = 90°,\ \varepsilon = 0°$). This is due to the fact that the IRNSS satellites extension at this location is a bit larger in West–East direction compared to the South–North direction.

Integrating the IRNSS with GPS Block IIF, both the heading and elevation increase in precision. The improvement in heading standard deviation is more significant for the baseline orientation of ($\alpha = 90°,\ \varepsilon = 0°$) compared to ($\alpha = 0°,\ \varepsilon = 0°$). This can be explained as follows. The IRNSS satellites, for almost all the locations, have a stronger extension along the West–East direction than the South–North direction. As a result, the baseline orientation ($\alpha = 0°,\ \varepsilon = 0°$) has already a heading estimation with high precision which is not the case with the baseline orientation

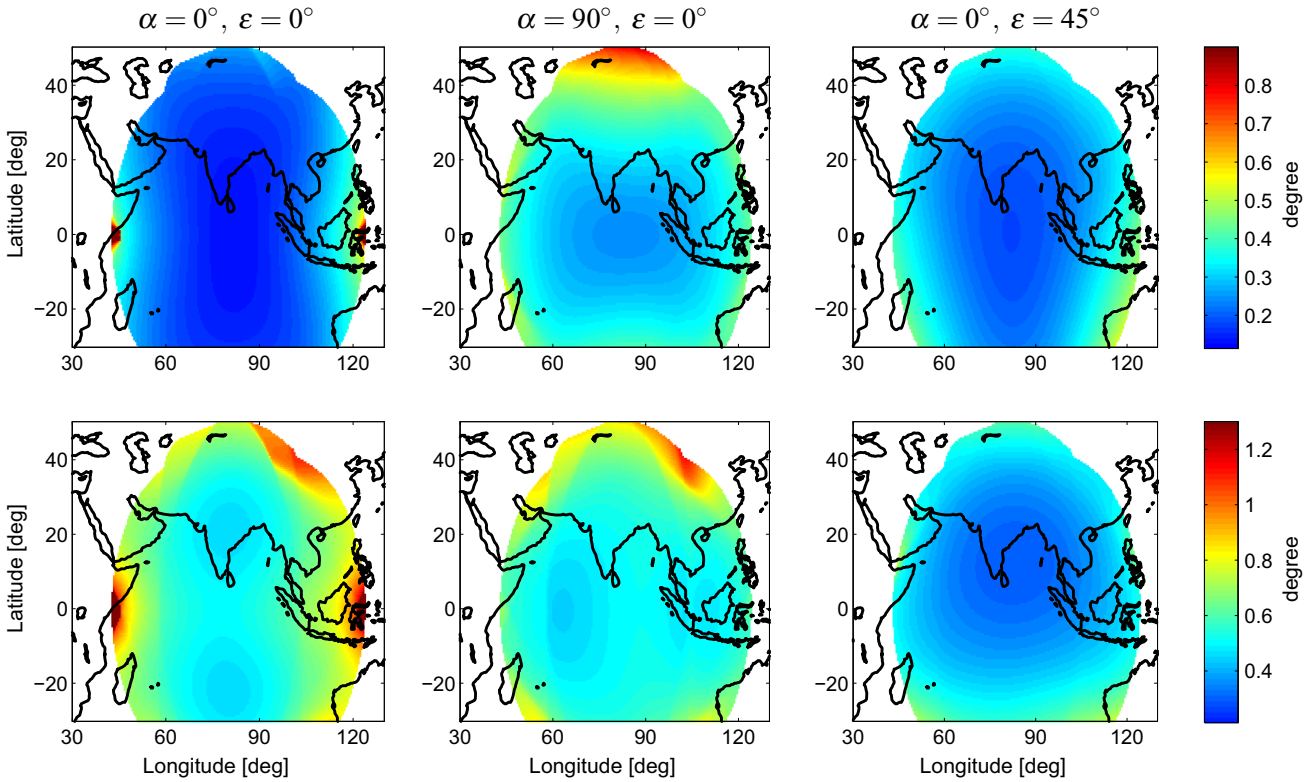

Fig. 12 Color map of day-averaged single-epoch ambiguity-resolved attitude angles standard deviation based on the standalone IRNSS L5, on DOY 167 of 2016 with 10° cutoff elevation. The results are computed assuming $\sigma_{\phi_I} = 2$mm and baseline length $l = 1$m, for the baseline orientations of, from left to right, ($\alpha = 0°,\ \varepsilon = 0°$), ($\alpha = 90°,\ \varepsilon = 0°$) and ($\alpha = 0°,\ \varepsilon = 45°$), respectively. *top* heading; *bottom* elevation. The *white areas* denote those locations excluded from our computations, due to having the poorer instantaneous MC-LAMBDA success rate than that of Perth

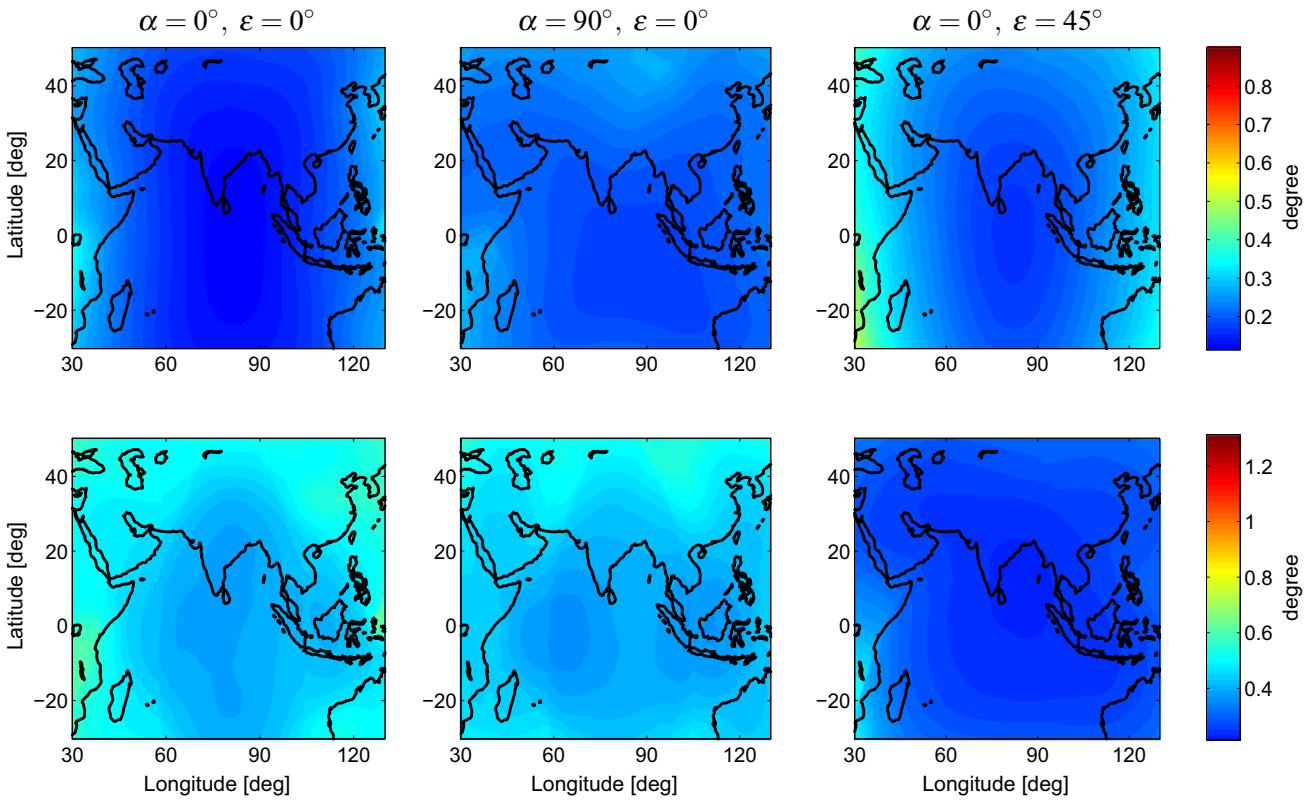

Fig. 13 Color map of day-averaged single-epoch ambiguity-resolved attitude angles standard deviation based on the IRNSS + GPS Block IIF L5, on DOY 167 of 2016 with 10° cutoff elevation. The results are computed assuming $\sigma_{\phi_I} = \sigma_{\phi_G} = 2$mm and baseline length $l = 1$m, for the baseline orientations of, from left to right, ($\alpha = 0°,\ \varepsilon = 0°$), ($\alpha = 90°,\ \varepsilon = 0°$) and ($\alpha = 0°,\ \varepsilon = 45°$), respectively. *top* heading; *bottom* elevation

($\alpha = 90°,\ \varepsilon = 0°$). Adding GPS Block IIF constellation to IRNSS enhances the South–North satellites extension, thus considerably improving heading precisions for the baseline orientation ($\alpha = 90°,\ \varepsilon = 0°$).

7 Conclusion

In this contribution, we presented the very first L5 attitude determination analyses of the fully operational IRNSS as a standalone system and also in combination with the fully operational GPS Block IIF. The noise characteristics of the L5 signal for both the IRNSS and GPS were assessed through the carrier-to-noise density, measurement precision and time correlation. It was shown that the GPS data have a significantly lower noise level than that of the IRNSS, particularly in case of the code data. The time correlation of both the constellations was shown to be negligible providing that the multipath impact is corrected for, even if 1-s data are used. Our analyses were conducted on an epoch-by-epoch basis, using both the multipath-corrected and original 1-s data collected by three stations at Curtin University, Perth, Australia.

A prerequisite for precise and fast attitude determination is the successful resolution of the DD ambiguities. Employing real data, we compared the performance of standard LAMBDA and MC-LAMBDA method for both a linear array of two antennas and a planar array of three antennas with the following body frames

$$\text{Linear array: } B = 6.15 \text{ m}$$

$$\text{Planar array: } B = \begin{bmatrix} 6.15 & 6.78 \\ 0 & 4.22 \end{bmatrix} \text{ m}$$

Based on the multipath-corrected data, when switching from LAMBDA to MC-LAMBDA, the standalone IRNSS instantaneous ambiguity resolution success rate was shown to increase significantly from 20.4 to 94.3% for the linear array and from 9.3 to 99.9% for the planar array. Upon integrating IRNSS with GPS Block IIF, the instantaneous MC-LAMBDA success rates of 99.8% and larger than 99.9% were achieved for the mentioned linear and planar array, respectively. For the original data, the mentioned success rates are marginally smaller.

Having investigated the ambiguity resolution performance, we then assessed the attitude angles precision for both the ambiguity-float and ambiguity-fixed scenarios. The orthonormality constraint of the rotation matrix, involved in the attitude observational model, is a nonlinear constraint of which the impact on the constrained baseline and attitude angles estimation was explained. The larger the standard deviation of the GNSS data and/or the shorter the baselines length, the more considerable the impact of the constraint nonlinearity, and the poorer the linear approximation will be.

Our ambiguity-fixed results showed that for the linear array oriented in South–North direction with the length of around $l = 6$ m, heading and elevation are estimable with the standard deviations of 0.04 and 0.09 degrees in case of standalone IRNSS and 0.02 and 0.05 degrees in case of IRNSS + GPS Block IIF. The higher precision of heading compared to the elevation was explained through the baseline orientation and satellites geometry. For the planar array, the ambiguity-fixed standard deviations for heading, elevation and bank were 0.03, 0.08 and 0.10 degrees in case of standalone IRNSS and 0.01, 0.04 and 0.06 degrees in case of IRNSS + GPS Block IIF.

For the ambiguity-fixed scenario, a good consistency was shown between our empirical outcomes and their *linearized* formal counterparts, implying that the easy-to-compute (linearized) formal values can indeed be used to predict the expected attitude determination performance. Therefore, we performed a formal analysis of the ambiguity-fixed attitude angles standard deviations over the IRNSS primary and secondary service area. Such an analysis was provided for those locations where the high instantaneous MC-LAMBDA success rates are guaranteed.

Our evaluations were based on the following setup: phase standard deviations $\sigma_{\phi_I} = \sigma_{\phi_G} = 2$mm, baseline length $l = 1$m, baseline orientations ($\alpha = 0°$, $\varepsilon = 0°$), ($\alpha = 90°$, $\varepsilon = 0°$) and ($\alpha = 0°$, $\varepsilon = 45°$). For such a setup, we illustrated the L5-based heading and elevation standard deviations on the basis of standalone IRNSS and IRNSS + GPS Block IIF. For other values of phase data precision and baseline length, these results will change according to (15). It was shown that the heading and elevation precision at a given location varies with changing baseline orientation, which was explained through the satellites geometry extension.

Switching from standalone IRNSS to IRNSS + GPS Block IIF, both the heading and elevation increase in precision. The improvement in heading standard deviation was shown to be more significant for the South–North-oriented baseline compared to the West–East-oriented baseline. This is due to the IRNSS satellites having a stronger extension along the West–East direction than the South–North direction for almost all the locations within its service area. As a result, the South–North-oriented baseline has already a heading estimation with high precision which is not the case with the West–East-oriented baseline. Adding GPS Block IIF to IRNSS enhances the South–North satellites extension, thus considerably improving heading precision for the West–East-oriented baseline.

Acknowledgements The second author is the recipient of an Australian Research Council (ARC) Federation Fellowship (Project Number FF0883188). This support is gratefully acknowledged.

Appendix: Nonlinearity of the GNSS attitude model

The orthonormality constraint of the rotation matrix R_q in (6) is a nonlinear constraint. Here, through simulation, we explain the impact of this nonlinearity on the estimation of the attitude angles. Considering the linear array of CUCC–CUBB, we simulated two sets of 10^4 baseline solutions, corresponding to the unconstrained ambiguity-float and ambiguity-fixed scenarios. They were generated from the normal distribution with the same mean (CUCC–CUBB baseline ground truth $\bar{b}$), but different variances. The variance matrix of the first set Q_1 is equal to the average formal variance matrix of the blue dots in Fig. 9a over the first 15,000 epochs, while the variance matrix of the second set is given by $Q_2 = \frac{\sigma_{\phi_I}}{\sigma_{p_I}} Q_1$.

As was previously mentioned, for the single-baseline scenario, the orthonormality constraint of the rotation matrix is equivalent to the length constraint on the baseline vector, i.e., $||x|| = l$. It indicates that the baseline vector is constrained to lie on a sphere with known radius of l. Imposing the baseline-length constraint, we estimated the heading and elevation of the CUCC–CUBB baseline based on the two sets of simulated data. Figure 14 shows the corresponding histograms of the estimated attitude angles, corrected for the ground truth, on the basis of the samples with the variance matrix Q_1 (a) and samples with the variance matrix Q_2 (b). Given the *linearized* formal standard deviations of the estimated angles, we computed the corresponding zero-mean normal PDF (probability density function) which are indicted by the red curves in Fig. 14.

The histograms in Fig. 14a demonstrate an asymmetric behavior. From these two histograms, it can be seen that the empirical density of the errors of the estimated angles at negative values is not the same as that at positive values, implying that the estimated angles are biased. This bias is called the nonlinearity bias which was already recognized, in the baseline domain, in the gray scatter plots in Fig. 10. Also, the deviation of these histograms from the red normal curve indicates that looking at only the standard deviations of the attitude angles is not enough to find out the complete probabilistic behavior of their estimators. The histograms in Fig. 14b, in contrast, show a very good consistency with

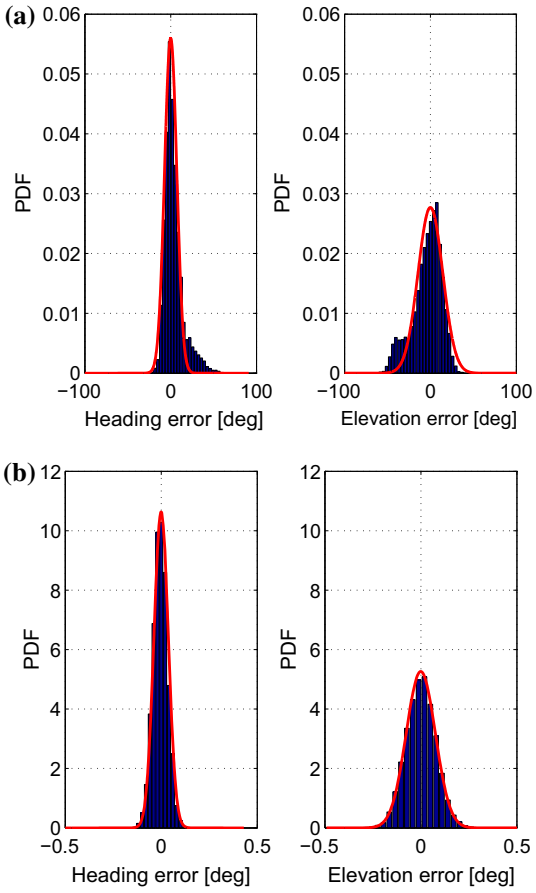

Fig. 14 *Histograms* of the heading (*left*) and elevation (*right*) estimation errors (*blue*) and their linearized formal counterparts (*red*). These results are computed based on 10^4 normally distributed baseline samples with the mean value of the CUCC–CUBB baseline ground truth and with two variance matrices Q_1 (**a**) and $Q_2 = \frac{\sigma_{\phi_I}}{\sigma_{p_I}} Q_1$ (**b**). Q_1 is equal to the average formal variance matrix of the *blue dots* in Fig. 9a over the first 15,000 epochs

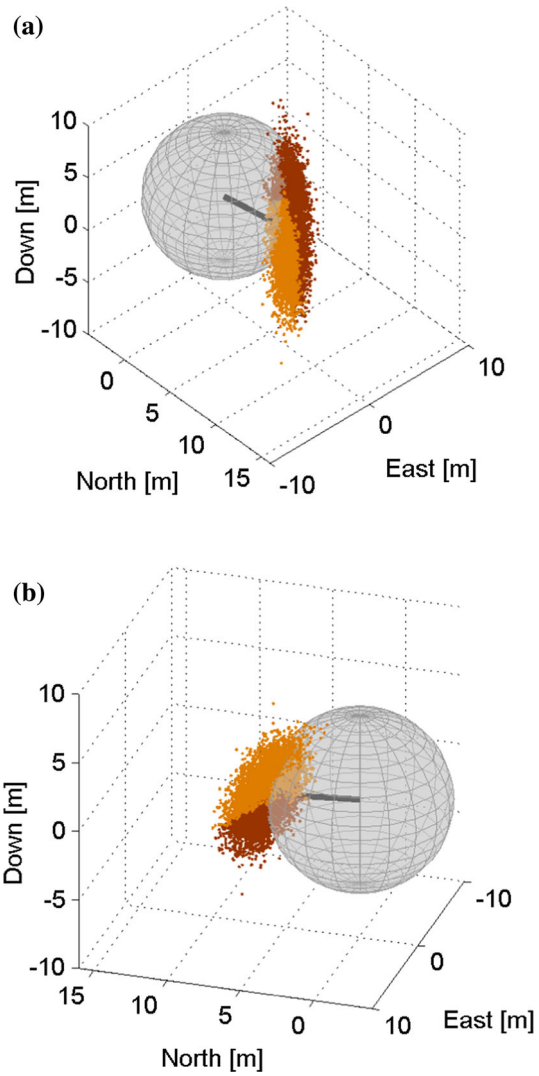

Fig. 15 Mapping the unconstrained ambiguity-float baseline solutions to their baseline-length-constrained counterparts. The scatter plot of 10^4 normally distributed baseline samples with the mean value of the CUCC–CUBB baseline ground truth and with the variance matrix of Q_1 (the average formal variance matrix of the blue dots in Fig. 9a over the first 15,000 epochs). The *gray vector* and the *sphere* denote, respectively, the baseline ground truth and the sphere with the radius of the CUCC–CUBB baseline length l. The *scatter plot* is split into two clusters. *light brown/dark brown* the points that upon constraining the baseline length result in negative/positive $\{*\}$ estimation errors. $\{*\}$: heading (**a**); elevation (**b**)

their corresponding normal PDF. This is due to the fact that these estimations are based on the very precise samples with the precision (Q_2) at the level of phase precision, where the nonlinearity of the attitude model can be neglected.

The signature of the attitude angles histograms is driven by the variance matrix of the simulated samples, hence the size, shape and orientation of their scatter plot. The asymmetric signature in Fig. 14a can therefore be explained through the specific orientation of the first set of simulated data scatter plot. Figure 15a, b shows the scatter plot of the first set of the simulated samples each of which is split into two clusters (*light/dark brown*) based on two different criteria. Clusters in panel (a), upon constraining the baseline length, result in heading estimation errors either of negative (light brown) or positive (dark brown) values, while clusters in panel (b) are the counterparts of those in panel (a) for the elevation estimation errors. It can be seen that the two clusters are not symmetric in any of the two panels. This explains the asymmetric behavior of the histograms in Fig. 14a.

In Fig. 15a/b, the light brown and the dark brown clusters are separated by a two-dimensional manifold being the locus of the points which, upon constraining the baseline length, result in the heading/elevation estimation errors equal to zero. The intersection of these two manifolds then accommodates the points which, upon constraining the baseline length, are mapped to the baseline ground truth $\bar{b}$. This intersection is described by a straight line given by

$$b_o = \left(I_3 + k\, Q_{\hat{b}\hat{b}}\right)\, \bar{b};$$

$$k \in \mathbb{R}: \ \left|\left|b_o - \bar{b}\right|\right|^2_{Q_{\hat{b}\hat{b}}} \leq ||b_o - b||^2_{Q_{\hat{b}\hat{b}}} \qquad \forall\, b \in \mathbb{S}^3(l) \tag{17}$$

where $\mathbb{S}^3(l)$ is the set of points on the circumference of a three-dimensional zero-centered sphere with the radius of l. Proof is as follows. Given the unconstrained ambiguity-float baseline solution $\hat{b}$, its baseline-length-constrained counterpart is given by

$$\hat{\hat{b}} = \underset{\substack{||b|| = l \\ b \in \mathbb{R}^3}}{\operatorname{argmin}} \ \left|\left|\hat{b} - b\right|\right|^2_{Q_{\hat{b}\hat{b}}} \tag{18}$$

which, from geometrical point of view, is the point where the ellipsoid $\mathbb{E}^3 = \{b \in \mathbb{R}^3 |\ ||\hat{b} - b||^2_{Q_{\hat{b}\hat{b}}} = \text{constant}\}$ just touches the sphere $\mathbb{S}^3(l)$ (Teunissen 2010). This indicates that the gradient vectors of the mentioned ellipsoid and sphere will be parallel at point $\hat{\hat{b}}$. Therefore to find the locus of the points $b_o \in \mathbb{R}^3$ for which $\hat{\hat{b}} = \bar{b}$, the gradient vector of the corresponding ellipsoid $\mathbb{E}^3$ and sphere $\mathbb{S}^3(l)$ at $\bar{b}$ should be set parallel to each other, i.e.,

$$Q^{-1}_{\hat{b}\hat{b}} \left(b_o - \bar{b}\right) = k\, \bar{b} \tag{19}$$

where k is a scalar. Equation (19) can be worked out to

$$b_o = \left(I_3 + k\, Q_{\hat{b}\hat{b}}\right)\, \bar{b} \tag{20}$$

With changing k, (20) describes a straight line which is parallel to $Q_{\hat{b}\hat{b}}\bar{b}$ and passes through $\bar{b}$. Note the values of k should result in $\bar{b}$ being the solution of (18) for $\hat{b} = b_o$ given by (20). Therefore, k follows from

$$k \in \mathbb{R}: \ \left|\left|b_o - \bar{b}\right|\right|^2_{Q_{\hat{b}\hat{b}}} \leq ||b_o - b||^2_{Q_{\hat{b}\hat{b}}} \qquad \forall\, b \in \mathbb{S}^3(l) \tag{21}$$

□

References

Amiri-Simkooei AR, Tiberius CCJM (2007) Assessing receiver noise using GPS short baseline time series. GPS Solut 11(1):21–35

Babu R, Mula P, Ratnakara SC, Ganeshan AS (2015) IRNSS satellite parameter estimation using combination strategy. Glob J Sci Front Res 15(3):87–95

de Bakker PF, Tiberius CCJM, van der Marel H, van Bree RJP (2012) Short and zero baseline analysis of GPS L1 C/A, L5Q, GIOVE E1B, and E5aQ signals. GPS Solut 16(1):53–64

Buist PJ (2007) The baseline constrained LAMBDA method for single epoch, single-frequency attitude determination applications. In: Proceedings of the 20th international technical meeting of the satellite division of The Institute of Navigation (ION GNSS 2007), ION, pp 2962–2973

Chandrasekhar MV, Rajarajan D, Satyanarayana G, Tirmal N, Rathnakara SC, Ganeshan AS (2015) Modernized IRNSS broadcast ephemeris parameters. Control Theory Inform 5(2):1–9

Cohen C (1992) Attitude determination using GPS. Ph D Thesis Stanford University

Euler HJ, Goad CC (1991) On optimal filtering of GPS dual frequency observations without using orbit information. Bull Geod 65(2):130–143

Ganeshan AS, Ratnakara SC, Srinivasan N, Rajaram B, Tirmal NKA (2015) First position fix with IRNSS. Inside GNSS 10(4):48–52

Giorgi G, Buist PJ (2008) Single-epoch, single-frequency, standalone full attitude determination: experimental results. In: Proceedings of the fourth ESA workshop on satellite navigation user equipment technologies, NAVITEC. ESA-ESTEC, The Netherlands

Giorgi G, Teunissen PJG, Buist PJ (2008) A search and shrink approach for the baseline constrained LAMBDA method: experimental results. In: Yasuda A (ed) Proceedings of international symposium on GPS/GNSS, Tokyo University of Marine Science and Technology, pp 797–806

Giorgi G, Teunissen PJG, Verhagen S, Buist PJ (2010) Testing a new multivariate GNSS carrier phase attitude determination method for remote sensing platforms. Adv Space Res 46(2):118–129

GPS Directorate (2011) Navstar GPS space segment/user segment L5 interfaces (IS-GPS-705B). Technical report

Harville DA (1997) Matrix algebra from A statistician's perspective. Springer, New York

Hauschild A, Grillmayer G, Montenbruck O, Markgraf M, Vörsmann P (2008) GPS based attitude determination for the flying laptop satellite. In: Small satellites for earth observation, Springer, pp 211–220

Hide C, Pinchin J, Park D (2007) Development of a low cost multiple GPS antenna attitude system. In: Proceedings of ION GNSS, pp 88–95

Hodgart MS, Purivigraipong S (2000) New approach to resolving instantaneous integer ambiguity resolution for spacecraft attitude determination using GPS signals. In: Proceedings of IEEE position location and navigation symposium, IEEE, pp 132–139

ISRO (2014) INDIAN REGIONAL NAVIGATION SATELLITE SYSTEM: signal in space ICD for standard positioning service, Version 1.0. ISRO Satellite Centre, June 2014

ISRO (2016) PSLV-C33/IRNSS-1G. http://www.isro.gov.in/sites/default/files/pslv-c33-brochure.pdf, published April 2016. Accessed 1 June 2016

Kuipers JB (2002) Quaternions and rotation sequences. Princeton University Press, Princeton

Kumari A, Samal K, Rajarajan D, Swami U, Babu R, Kartik A, Rathnakara SC, Ganeshan AS (2015) Precise modeling of solar radiation pressure for IRNSS satellite. J Nat Sci Res 5(3):35–43

Li Y, Zhang K, Roberts C, Murata M (2004) On-the-fly GPS-based attitude determination using single- and double-differenced carrier phase measurements. GPS Solut 8(2):93–102

Lu G (1995) Development of a GPS multi-antenna system for attitude determination. Ph.D. Thesis University of Calgary

Madsen J, Lightsey EG (2004) Robust spacecraft attitude determination using global positioning system receivers. J Spacecr Rockets 41(4):635–644

Magnus JR, Neudecker H et al (1995) Matrix differential calculus with applications in statistics and econometrics. Wiley, New York

Montenbruck O, Steigenberger SR (2015) IRNSS orbit determination and broadcast ephemeris assessment. In: Proceedings of the 2015 international technical meeting of the institute of navigation, Dana Point, California, January 2015, pp 185–193

Nadarajah N, Khodabandeh A, Teunissen PJG (2015) Assessing the IRNSS L5-signal in combination with GPS, Galileo, and

QZSS L5/E5a-signals for positioning and navigation. GPS Solut 20(2):289–297
Odijk D, Teunissen PJG (2008) ADOP in closed form for a hierarchy of multi-frequency single-baseline GNSS models. J Geod 82(8):473–492
Odijk D, Teunissen PJ (2013) Characterization of between-receiver GPS-Galileo inter-system biases and their effect on mixed ambiguity resolution. GPS Solut 17(4):521–533
Odijk D, Teunissen PJG, Huisman L (2012) First results of mixed GPS + GIOVE single-frequency RTK in Australia. J Spat Sci 57(1):3–18
Odijk D, Nadarajah N, Zaminpardaz S, Teunissen PJG (2016) GPS, Galileo, BDS, QZSS and IRNSS differential ISBs: estimation and application. GPS Solut. doi:10.1007/s10291-016-0536-y
Park C, Teunissen PJG (2003) A new carrier phase ambiguity estimation for GNSS attitude determination systems. In: Proceedings of international GPS/GNSS symposium, Tokyo, vol 8, pp 283–290
Park C, Teunissen PJG (2009) Integer least squares with quadratic equality constraints and its application to GNSS attitude determination systems. Int J Control Autom 7(4):566–576
Psiaki ML (2006) Batch algorithm for global-positioning-system attitude determination and integer ambiguity resolution. J Guid Control Dyn 29(5):1070–1079
Tegedor J, Øvstedal O (2014) Triple carrier precise point positioning (ppp) using gps l5. Surv Rev 46(337):288–297
Teunissen P (2006) The LAMBDA method for the GNSS compass. Artif Satell 41(3):89–103
Teunissen P (2007) A general multivariate formulation of the multi-antenna GNSS attitude determination problem. Artif Satell 42(2):97–111
Teunissen PJ (1995) The least-squares ambiguity decorrelation adjustment: a method for fast GPS integer ambiguity estimation. J Geod 70(1–2):65–82
Teunissen PJ (2010) Integer least-squares theory for the GNSS compass. J Geod 84(7):433–447
Teunissen PJ, Giorgi G, Buist PJ (2011) Testing of a new single-frequency GNSS carrier phase attitude determination method: land, ship and aircraft experiments. GPS Solut 15(1):15–28
Teunissen PJG (1989) Estimation in nonlinear models, II. Hotine-Marussi symposium on mathematical geodesy, Pisa, Italy, June 5–8
Teunissen PJG (1997) A canonical theory for short GPS baselines. Part I: the baseline precision. J Geod 71(6):320–336
Teunissen PJG (1998) Success probability of integer gps ambiguity rounding and bootstrapping. J Geod 72(10):606–612
Teunissen PJG (1999) An optimality property of the integer least-squares estimator. J Geod 73(11):587–593
Teunissen PJG (2012) The affine constrained GNSS attitude model and its multivariate integer least-squares solution. J Geod 86(7):547–563
Teunissen PJG, Amiri-Simkooei AR (2008) Least-squares variance component estimation. J Geod 82(2):65–82
Thoelert S, Montenbruck O, Meurer M (2014) IRNSS-1A: signal and clock characterization of the Indian regional navigation system. GPS Solut 18(1):147–152
Wang B, Miao L, Wang S, Shen J (2009) A constrained LAMBDA method for GPS attitude determination. GPS Solut 13(2):97–107
Zaminpardaz S, Teunissen PJG, Nadarajah N (2016a) GLONASS CDMA L3 ambiguity resolution and positioning. GPS Solut. doi:10.1007/s10291-016-0544-y
Zaminpardaz S, Teunissen PJG, Nadarajah N (2016b) IRNSS standalone positioning: first results in Australia. J Spat Sci 61(1):5–27